minerals

MDPI

Article

Activation of Dolomite Flotation by Ferrous Hydroxide and Carbonate

Haiping Zhao [1,2,3], Xiaopeng Niu [1,2], Bingxu Dong [4], Xianbing Jia [1,2] and Renman Ruan [1,2,*]

[1] CAS Key Laboratory of Green Process and Engineering, Institute of Process Engineering, Chinese Academy of Sciences, Beijing 100190, China
[2] National Engineering Research Center of Green Recycling for Strategic Metal Resources, Chinese Academy of Sciences, Beijing 100190, China
[3] University of Chinese Academy of Sciences, Beijing 100049, China
[4] Postdoctoral Research Station, Guosen Securities Co., Ltd., Shenzhen 518001, China
* Correspondence: rmruan@ipe.ac.cn

Abstract: The major problem with Carlin-type gold deposit flotation is that the high dolomite content in the concentrate decreases the quality of gold. Further, the activation mechanisms involved in dolomite flotation are still not fully understood. Herein, the correlation of Fe^{2+} conversion with xanthate adsorption and dolomite flotation was investigated to reveal the effect of dolomite embedded with pyrite. Flotation tests suggested that Fe^{2+} rather than Fe^{3+} improved the floatability of dolomite from 20% to 45%. Contact angles and thermodynamic tests indicated that the hydrophobicity of Fe^{2+}-modified dolomite corresponds to the adsorption of xanthate. Importantly, time-of-flight secondary ion mass spectroscopy (Tof-SIMS) and x-ray photoelectron spectroscopy (XPS) attributed the activation of dolomite flotation to the formation of $Fe(OH)_2$ and $FeCO_3$. The coordination model of flotation successfully elucidated the selective adsorption of xanthate between $Fe(OH)_2$, $FeCO_3$ and FeOOH surfaces. The density function theory (DFT) simulation calculation was performed to identify the reaction rate at the atomic level, and the density of states (DOS) was also conducted to verify the conclusions at the electronic level. This study presents important surface chemistry evidence for understanding and regulating the poor selectivity in the flotation of Carlin-type gold deposits.

Keywords: ferrous hydroxide/carbonate; dolomite activation; coordination model; carlin-type gold deposits; flotation

check for updates

Citation: Zhao, H.; Niu, X.; Dong, B.; Jia, X.; Ruan, R. Activation of Dolomite Flotation by Ferrous Hydroxide and Carbonate. *Minerals* **2023**, *13*, 200. https://doi.org/10.3390/min13020200

Academic Editors: Jenna Poonoosamy and Felix Brandt

Received: 19 December 2022
Revised: 13 January 2023
Accepted: 19 January 2023
Published: 30 January 2023

Copyright: © 2023 by the authors. Licensee MDPI, Basel, Switzerland. This article is an open access article distributed under the terms and conditions of the Creative Commons Attribution (CC BY) license (https://creativecommons.org/licenses/by/4.0/).

1. Introduction

In the formation of Carlin-type gold ores, the hydrothermal fluids disperse and diffuse through the dolomitic beds, which increased the dolomite proportion in the Carlin-type gold deposit, and deteriorated gold recovery [1]. Considering the natural hydrophobicity of sulfide ores, xanthate flotation is the most common choice to separate gold ores from dolomite. Further, it is widely accepted that dolomite maintains the pulp pH, accelerates the oxidation of sulfide ores, complicates the pulp environment, and destroys the selectivity of sulfide mineral flotation. As previously reported, many studies have focused on the flotation performance of pyrite. Flotation recovery of auriferous pyrite with low, medium, and high dolomite content is 51.3%, 38.6%, and 36.7%, respectively; meanwhile, with the increase in pyrite content from 1.2% to 3%, the floating rate of dolomite increases from 8.6% to 18.7% [2,3]. However, the flotation performance of dolomite when embedded with pyrite is not fully understood. Herein, the investigation of dolomite effects in xanthate solution is compulsory to provide substantial perspectives in restoring the selectivity between the valuable minerals and associated carbonatite gangues.

Dolomite precipitation and dissolution have been extensively studied, called the "dolomite problem" [4–6]. The dissolved ions can undergo hydrolysis, complexation, adsorption, and precipitation reactions, which can deteriorate the interactions between

reagents and minerals [7]. XPS analysis shows that the inhibition effect of Mg^{2+} on pyrite flotation is dominated by the positively charged $Mg(OH)_2$, which precipitated on the negatively charged pyrite surface, thus hindering collector-selective adsorption [8,9]. In general, the stability of complex is much higher than those of hydrolysate [10]. Therefore, many investigations focused on the interactions between complexes and dolomite. For example, the alkyl hydroxamic acid can be used to selectively separate dolomite and ankerite, which was attributed to the stronger covalent character between Fe and head oxygen atoms [11]. In contrast, the competitive adsorption of $CaOH^+$ and DDTC on pyrite surface was a better explanation for the decreased pyrite recovery at high pH [12]. Selectivity of complexes provides a corresponding potential in regulating dolomite flotation. In recent decades, many works aimed to explore dolomite depressants have been performed. Xanthan gum [13], BATPA [14], sodium hexametaphosphate [3] and NSFC [15] can selectively adsorb on the dolomite surface through the interactions between carboxyl/hydroxyl groups and Ca/Mg sites, which inhibited the collector (sodium oleate) adsorption, and rendered the surface hydrophilicity [2,13,16]. However, those depressants suffered from the disadvantages of low selectivity, severe water pollution, and sensitivity to slimes in xanthate flotation [17]. Furthermore, there have not been numerous reports concerned with the interactions between dolomite and xanthate. As a result, the key to revealing the conflicting results and developing the selectivity of the Carlin-type gold deposit lies in the behavior of dolomite in the process of xanthate flotation.

Due to the oxidation of pyrite, and consumption of grinding medium, Fe^{2+} and Fe^{3+} inevitably exist in the pulp of the natural flotation system [18]. A limited improvement of dolomite recovery by Fe^{3+} was presented, which is difficult to control in experiments. Hence, research on the effects of Fe^{2+} is essential to regulate the selectivity of dolomite flotation. Fe^{2+} is widely used in chemical activation in the degradation of heavy metals [19], the treatment of organic wastewater [10], and the modification of mineral surfaces [20]. This certainly includes some attempts in flotation. Liberated ferrous ions from the oxidation of pyrite were adsorbed and retained easily on mineral surfaces due to the pH-buffering role of dolomite [21–23], which can cause mineral activation or inhibition during the flotation process [24]. Different schematics such as generating compounds and competition adsorption were proposed to describe the behavior of Fe^{2+} in mineral flotation [25]. XPS and FTIR results described that the displacement of Sn^{4+} with Fe^{2+} allows the formation of Fe-SHA compounds, thus increasing its recovery [26], and a similar mechanism was utilized to interpret the extra floatability of quartz [18,25]. Considering the affinities between reagents and mineral surfaces, competitive adsorption plays a crucial role in dominating flotation performance. Through the $Fe(OH)^{2+}$ adsorption, the addition of Fe^{2+} can activate sphalerite surfaces [27]. This agrees well with the conclusion drawn by removing EDTA-Pb by Fe^{3+} [10]. Although remarkable works have trickled into the open literature to mitigate the negative effects of dolomite on sulfide ore flotation, knowledge about the correlation of Fe^{2+}, dolomite, and xanthate is limited due to the lack of intermediate product evidence during flotation. The proposed mechanisms could not explain several phenomena. For example, dolomite recovery increased with the increase in initial pyrite contents [27]. Further, few researchers paid attention to the structural properties of dolomite, the most critical factors in determining the floatability. Knowledge on Fe^{2+}-modified dolomite flotation in xanthate-containing solutions is still in need of development.

This paper aims to explore the effects of Fe^{2+} adsorption and conversion on the dolomite surface in xanthate-containing systems. The flotation performance of dolomite as the initial Fe^{2+} concentration was tested. Contact angles and thermodynamic analysis were studied to correlate the hydrophobicity of Fe^{2+}-modified dolomite with xanthate adsorption. Grazing incident x-ray diffraction (GI-XRD), XPS, and Tof-SIMS were adopted to identify the activated species of modified dolomite. The coordination model of mineral flotation and DFT calculation were used to further reveal the reaction mechanism. The conclusions are expected to provide important surface evidence for understanding the activation of dolomite when embedded with pyrite in Carlin-type gold deposits.

2. Materials and Methods

2.1. Materials

The collector sodium butyl xanthate (SBX) [$C_4H_9OCS_2Na$, 80%] was obtained from Aladdin Industrial Corporation. Iron (II) sulfate heptahydrate ($FeSO_4 \cdot 7H_2O$, 99%) and Iron (III) sulfate heptahydrate ($Fe_2(SO_4)_3 \cdot xH_2O$, 99%) were purchased from Xilong Scientific Co., Ltd. Sodium hydroxide (NaOH, 98%) and hydrochloric acid (HCl) were adopted as pH regulators. Terpenic oil was used as the frother.

2.2. Sample Preparation

High-purity natural dolomite samples were sampled from Haicheng, Dongbei Province. GI-XRD (As illustrated in Figure S1) and composition results demonstrated 99.2% purity of dolomite (21.53% MgO).

The natural dolomite samples were crushed using a New Zealand crusher to collect the −2 mm particles. Then, the collected samples were vacuum packaged to minimize further contamination.

For contact angle measurements, GI-XRD tests, and XPS etching analysis, the minerals were cut into square flakes approximately 10 × 10 × 3 mm, and sequentially polished using 800, 3000, 5000, 7000 mesh abrasive paper underwater. Next, the flakes were rinsed in ethanol, ultrasonically processed for 1 min to further remove the impurity, and dried with high-purity nitrogen.

The powder samples were ground using an ultrafine grinding machine with a zirconia ball and then wet screened (ethanol) to collect −5 μm particles for the zeta potential and FTIR tests, and −30 + 20 μm size fractions for thermodynamic tests.

2.3. Micro-Flotation Tests

A 0.5 L mechanical single-trough flotation machine was used to conduct the flotation tests. The impeller speed and aeration rate were fixed at 2000 r/min, and 30 L/h, respectively. An amount of 100 g dolomite was ground in a 6.5 L ball mill (with 30 wt.% chromium content) to collect P90 of 60 μm sample (as depicted in Figure S2). Then, the collected pulp was transferred to the 0.5 L cell, and the suspension conditioned with $FeSO_4$ for 10 min, followed by treating with 10^{-3} M sodium butyl xanthate (SBX) for 10 min (The results in Figure S3 indicate this dosage is enough for dolomite flotation). Next, 80 g/t terpenic oil were added to form bubbles (1 min). Finally, the pulp was floated for 15 min, and the products were dried, and weighed. NaOH and HCl were employed to adjust the pH in the whole process. The recovery was calculated by mass balance. Five batch flotation tests were carried out under the same conditions, and the average value was submitted.

2.4. Contact Angle Measurements

The measurements of contact angles were carried out by pendant drops with a contact angle goniometer (DM-701, Kyowa Interface Science, Tokyo, Japan). One sample was processed sequentially to achieve the goal of monitoring the contact angle in situ. Firstly, the dolomite surface was exposed to $FeSO_4$ solutions of pH 8.5 with different times. Secondly, the obtained modified specimen was immersed in SBX solution, and equilibrium contact angles were recorded as the interaction time (keeping the flakes in solution at the fixed time, the surface dried with nitrogen, recording the contact angles, and repeated this process). At least five measurements were taken and averaged.

2.5. Thermodynamic Analysis

The 50 mg dolomite with different pretreatments was dried in vacuum. Next, the collected sample was inserted into the reaction calorimeter (RC1e, Mettler Instruments), which contained 4 mL DI water. After temperature correction (35 °C), 10^{-3} M SBX was added to the DI water. The reaction enthalpy between the modified dolomite surface and SBX was quantified by integrating the heat generation rate of the whole process (qr-hf).

2.6. XPS Analysis

X-ray photoelectron spectrometer (XPS, ESCALAB 250Xi, Thermo Fisher Scientific, Waltham, MA, USA) equipped with a monochromatic Al Kα X-rays (15 kV, 15 mA, 150 W, elliptical spot, and hemispherical analyzers) was employed to record the element spectrum of Fe 2p, O 1s, and C 1s for determining the valence state and element proportion. The energy resolution is 0.5 eV, the *glmix* (Fe) is 84%, and *glmix* (O) is 80%. The analysis chamber has a pressure of 2.31×10^{-8} Pa. Avantage v5.938 was selected to execute the peak fitting. All the spectra were charged with 284.8 eV C1s peak, and the Smart distracting background method was performed.

The XPS analysis samples were derived from the flotation process, filtered, frozen, and dried with a lyophilizer. After that, the target samples were immediately transported to the analysis chamber.

2.7. Time-of-Flight Secondary Ion Mass Spectrometry (Tof-SIMS) Tests

Tof-SIMS V (ION-TOF GmbH, German) equipped with enriched Bi^+ ion beam (25 kV) was used for sputtering and ionizing species of interested area on sample surface. The designed raster size is 200 × 200 μm (with 100 s acquisition time). The proportion of the surface components was expressed as the reported positive and negative secondary ion intensities. Data submitted were normalized by the total ion intensity.

Samples from the flotation process were removed from the solution, filtered, frozen, and dried with a lyophilizer. Finally, the collected samples were immediately transported into the Tof-SIMS instrument.

2.8. Computational Methods

We have adopted the Material studio to perform all density function theory (DFT) calculations within the CASTEP module. The nucleus and valence electrons were described by the projector augmented wave (PAW) method [28]. Generalized gradient approximation with the Perdew–Burke–Ernzerhof factor (GGA-PBE) was selected in all the calculations [29–31]. The DFT-D2 empirical correction method was adopted to describe the van der Waals force. Flake thicknesses and adsorption site (Ca/Mg/Fe) were tested to determine the most stable adsorption structure. Consequently, Monkhorst–Pack k-points of 4 × 2 × 1, 2 × 2 × 1, and 1 × 1 × 1 were applied for the calculations of $CaMg(CO_3)_2$, $Fe(OH)_2$ (with 400 eV cut-off energy) and $FeCO_3$ (with 450 eV cut-off energy) substrates, respectively, and the atoms at bottom were fixed in all the calculations. The optimized lattice parameters for $CaMg(CO_3)_2$ (101) surface are: a = 7.86210 Å, b = 9.79140 Å, c = 22.67490 Å. For the $Fe(OH)_2$ (101) surface: a = 11.40060 Å, b = 9.94500 Å, and c = 22.86470 Å. Additionally, for the $FeCO_3$ (100) surface: a = 14.06610 Å, b = 15.37300 Å, and c = 22.24697 Å. In particular, the AFM of Fe initial magnetic moment in $FeCO_3$ was set to −5 or +5 μB. The xanthate and water molecular adsorption energy E_{ads} on the $CaMg(CO_3)_2$, $Fe(OH)_2$, and $FeCO_3$ surfaces were calculated by the following equations:

$$E_{ads} = E_{(sub+adsorbent)} - E_{(sub)} - E_{(reference)} \quad (1)$$

where $E_{(sub+adsorbent)}$ and $E_{(sub)}$ are the total energy of the substrate surface with and without R or H_2O adsorption, respectively, and $E_{(reference)}$ is the total energy of R or H_2O molecule in the gas phase.

3. Results and Discussion

3.1. Floatability of Fe^{2+}-Modified Dolomite

Dolomite flotation was performed to investigate the effect of Fe^{2+} and Fe^{3+}. Results are depicted in Figure 1. As noted, there are not any obvious differences in dolomite recovery with the addition of Fe^{3+}. Meanwhile, Fe^{2+} showed a favorable influence on the flotation performance of dolomite (water recovery tests (Figure S4) were also performed to exclude the possibility of foam entrainment). As depicted in Figure 1, dolomite recovery increased

from 20% to 40% as the initial Fe^{2+} concentration increased from 0 to 5×10^{-3} M. With increasing Fe^{2+}, the increase in dolomite recovery gradually slowed down with 45% at 5×10^{-2} M Fe^{2+}. This agrees well with the previous results [2,9,32], where a substantially increasing flotation grade and almost constant recovery of dolomite in the presence of Fe was reported. They attributed this extra floatability to the oxidation of xanthate, which was believed to be beneficial for the reduction of ferric hydroxides to ferrous species [33]. However, there is limited evidence on this reduction process and its correlation with recovery, which is among the main points in this paper. Considering that the mineral oxidation and precipitation of Ca^{2+} and Mg^{2+} under high-alkali conditions will deteriorate the selectivity in the Fe^{2+}-bearing dolomite flotation [34], pH 8.5 is adopted for further investigation.

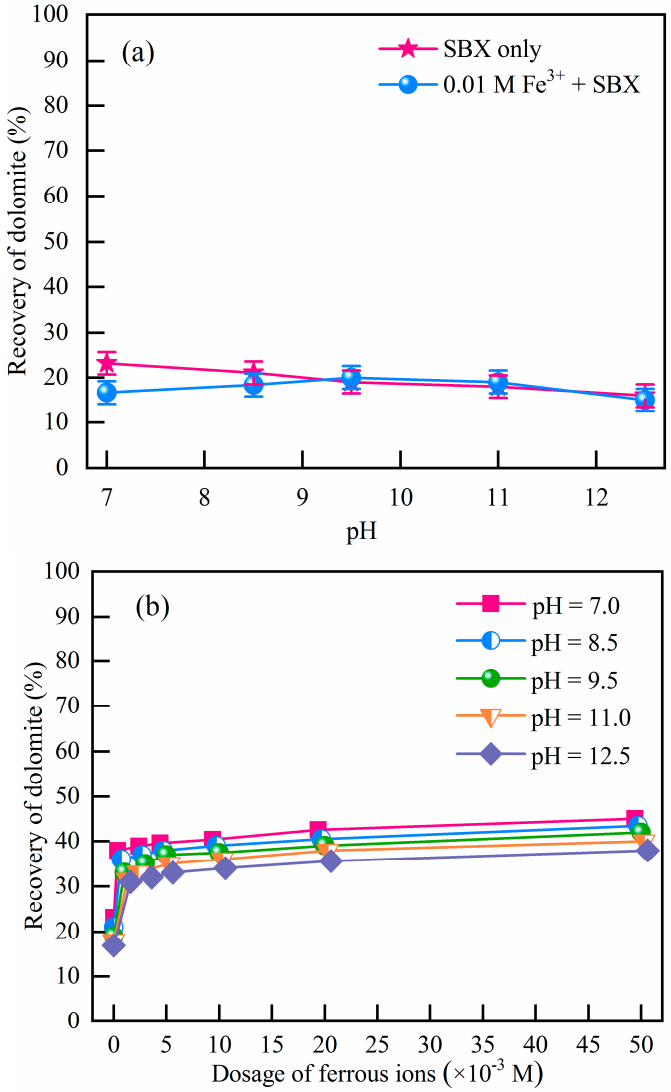

Figure 1. Floatability of dolomite with the addition of Fe^{3+} (**a**), and Fe^{2+} (**b**) (c(SBX) = 10^{-3} M).

3.2. Assessment of Hydrophobicity

Contact angles of dolomite treated with xanthate-containing solutions in Figure S5 show that the hydrophobicity is much less affected with increasing immersion time, which demonstrates the weak interactions between dolomite and xanthate. Figure 2 shows the contact angle of the dolomite surface with different pretreatments. As Figure 2a shows, the dolomite contact angle was 25° due to its natural hydrophobicity at pH 8.5, closed to 23°, described by other research [35]. When treated with Fe^{2+} (from 10^{-3} M to 10^{-2} M), contact angles of dolomite decreased to 7° due to the higher surface hydrophilicity. Many

works attributed this hydrophilicity to FeOOH precipitation [9,33]. Meanwhile, followed by the addition of SBX, the contact angles of dolomite with Fe^{2+} increased sharply from 7° to 43°, which suggests that the addition of Fe^{2+} is beneficial to the adsorption of SBX (it can provide a hydrophobicity surface because of the hydrophobic carbon chain). Contact angle results coincide with the flotation tests. To establish if a chemisorption process is involved, it is compulsory to detect if there are new chemical bonds by FTIR, thermodynamic tests, TGA, etc. Among them, thermodynamic data are the best reflection of the intensity of chemical reactions.

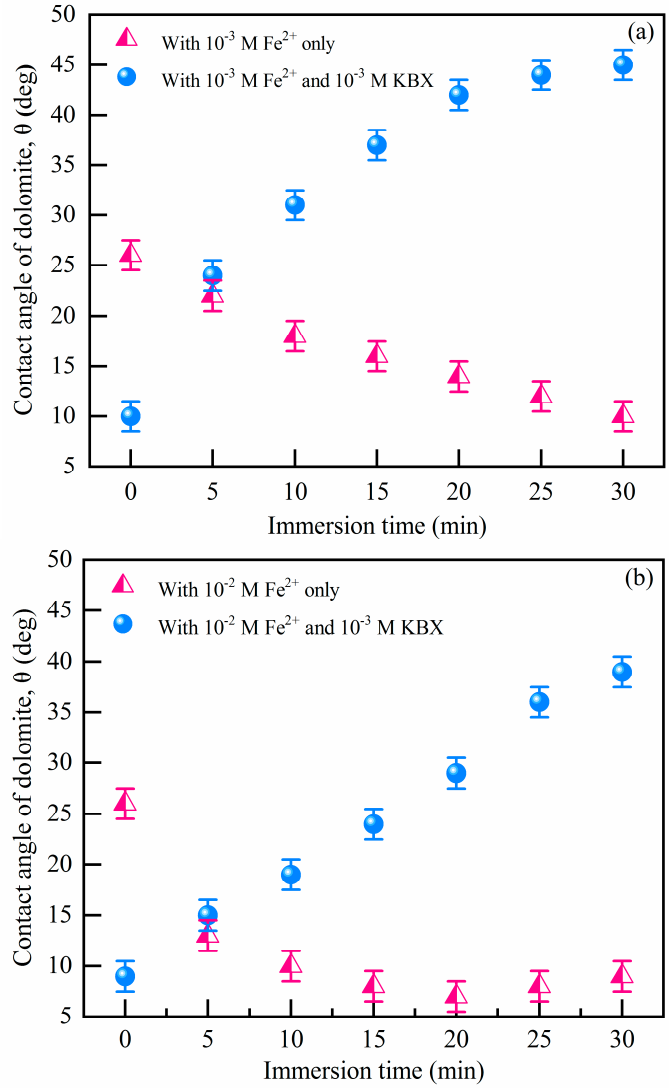

Figure 2. Contact angles of the dolomite surface in (**a**) 10^{-3} M Fe^{2+} and (**b**) 10^{-2} M Fe^{2+} solutions with different interaction times (pH = 8.5, c(SBX) = 10^{-3} M).

3.3. Identification of Xanthate Chemisorption

The adsorption heat is a good reflection of reagent adsorption capacity [36]. Figure 3 shows the chemical heat of modified dolomite with SBX. Obviously, dolomite cannot react with SBX, because the adsorption heat is just −0.6 J/g. The little adsorption heat is due to the contamination, which was introduced into the sample preparation [37]. Meanwhile, increasing the initial Fe^{2+} concentration from 10^{-3} M to 10^{-2} M decreases the adsorption heat value from −4.27 to −10.974 J/g, which reveals that the addition of Fe^{2+} promotes the chemisorption of xanthate on dolomite, and corresponds well with the conclusions of flotation and contact angle tests. The larger Fe^{2+} concentration was believed to be responsible for increasing the ferrous and iron hydroxide proportion [38]. Results of zeta

potential (Figure S6), FTIR (Figure S7), and Tof-SIMS (Figure S8) further confirmed that the adsorption of Fe^{2+} on dolomite provided the possibility of xanthate chemisorption.

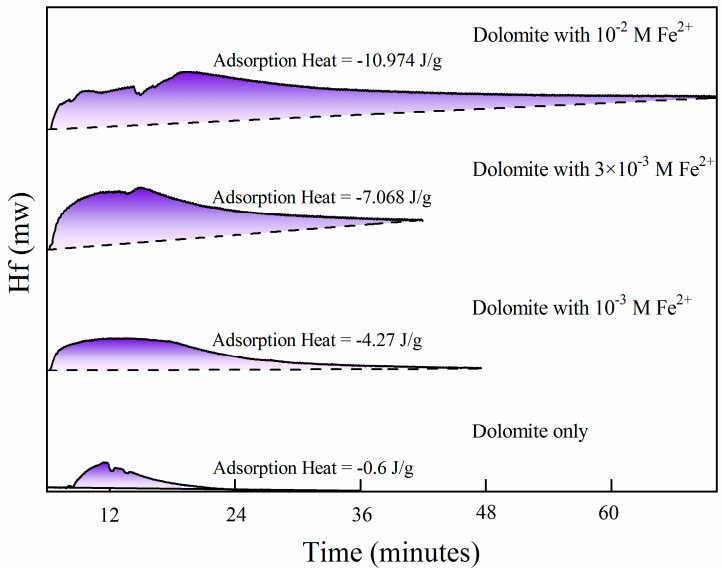

Figure 3. Adsorption heat of dolomite with SBX as the function of initial Fe^{2+} concentration (pH = 8.5, c(SBX) = 10^{-3} M SBX).

3.4. Characterization of Modified Surface Profile

3.4.1. Depth Profile

XPS etching is highly sensitive in recognizing species distribution [39,40]. XPS etching analyses aimed to provide the depth profile of the dolomite surface after treating with Fe^{2+} and SBX for density function theory (DFT) calculations. Results from Figure S10 show the chemical changes in the dolomite depth profile, and Figure 4 shows the dependence of the Fe and S atomic concentration on the etching time. As illustrated, few Fe and S atomics were observed on the control surface, whereas the amounts of sulfur (from SBX) and Fe absorbed on the dolomite surface increase with initial Fe^{2+} concentration throughout the studied depth range. Notably, after 9 min etching (115 nm vs. SiO_2), the atomic concentration of Fe and S was still reasonably stable, which indicates that the removal of Fe and S in dolomite was rather difficult due to the formation of a fairly thick adsorption layer in this flotation system. Additionally, it provides a better understanding of the poor separation performance between dolomite and pyrite in Carlin-type gold deposits.

3.4.2. Species Profile

The unsatisfactory separation efficiency was attributed to the complexation and transformation of ferrous and ferric ions [9,25]. Unfortunately, knowledge about the correlation of ionic adsorption, and precipitation with dolomite recovery is limited due to the lack of evidence on the intermediate products. The main conflict is the ambiguous states of Fe^{2+} in this flotation system.

Tof-SIMS is suitable for determining and quantifying surface components because of its high sensitivity in identifying elemental and molecules information of the outmost surface. In this study, Tof-SIMS tests were performed to clarify the main chemical fragments on the modified dolomite surface [41]. The normalized intensities of Fe species were calculated in Figure 5, and the relevant mass spectra were summarized and submitted in Figure S9. As illustrated in Figure 5a, the main detected fragments are $FeOH^+$ and FeH^+, which corresponds well with the previous investigations [41,42]. These fragments can be a possible proof of the existence of iron hydroxides and oxides. Further, considerable amounts $FeCO_2^+$, CO^-, CO_2^-, and CO_3^- fragments peaks are also observed. These are the characteristic peaks of $FeCO_3$ [43]. Therefore, the key to clarifying the ambiguous states of

Fe^{2+} lies in verifying the contribution of iron hydroxide, oxides, and $FeCO_3$ on the modified dolomite floatability.

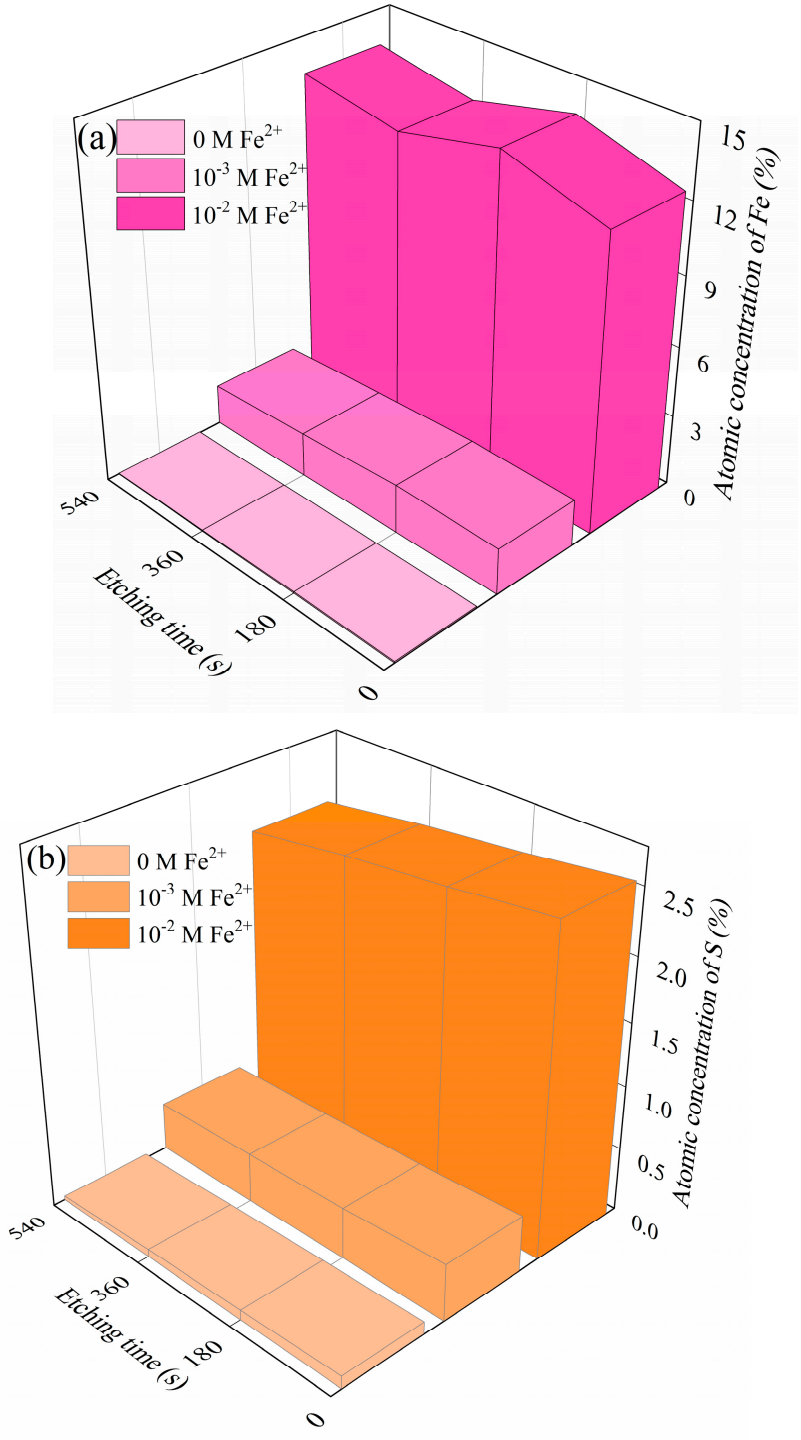

Figure 4. The depth profile for Fe (**a**) and S atomic percentage (**b**) of dolomite with and without the treatment of Fe^{2+} (c(SBX) = 10^{-3} M SBX).

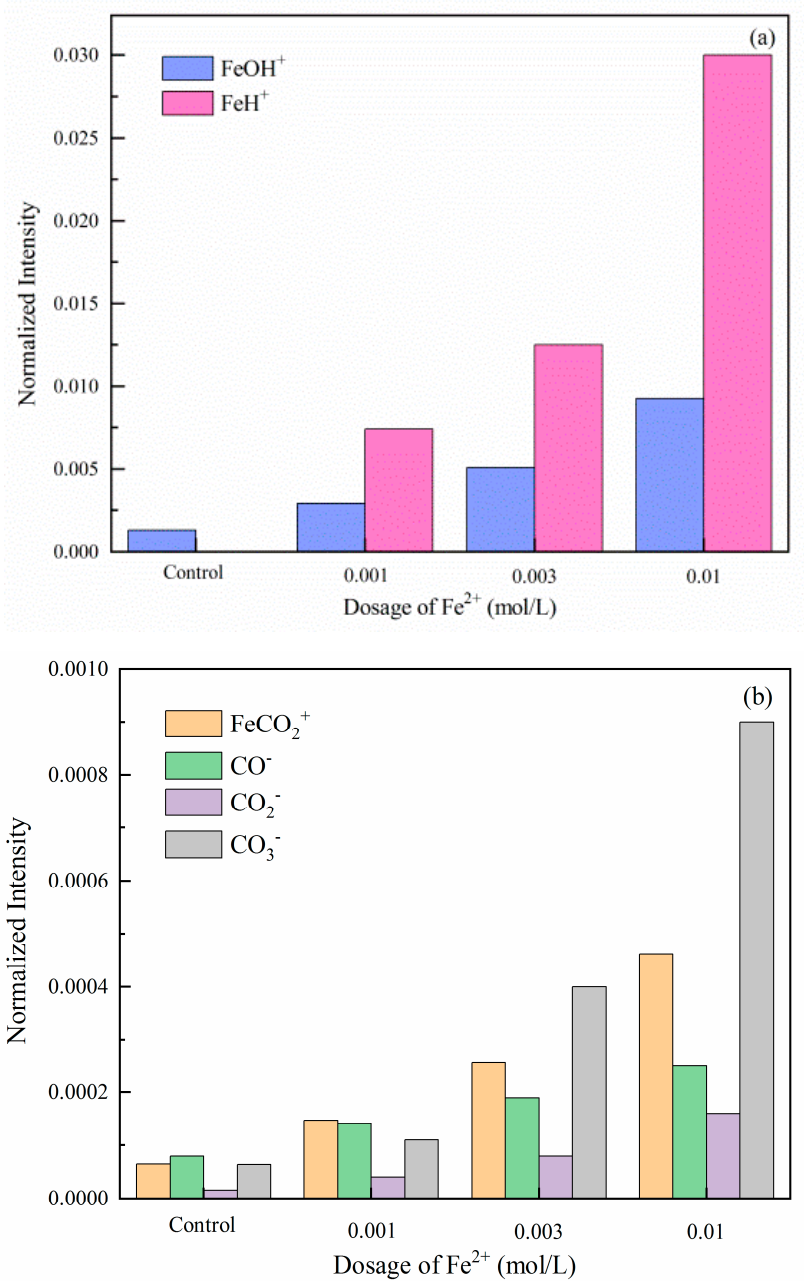

Figure 5. Normalized intensities of Fe-containing species ((**a**) $FeOH^+$ and FeH^+; (**b**) $FeCO^{2+}$, CO^-, CO^{2-} and CO^{3-}) (positive and negative secondary ions) on dolomite surfaces treated with Fe^{2+} (pH = 8.5).

For further identifying the components on the modified dolomite surface, Fe 2p, O 1s, and C 1s are recorded for valence state and compositional identification [44]. Because of the peak asymmetries, due to multiple splitting of Fe 2p spectra, the Fe 2p3/2 spectra were mainly analyzed to identify its valence state (the selected parameters are from [44]. The fitting peaks had a full width at half maximum (FWHM) between 1.3 and 1.5 eV.

Figure 6a shows the analysis results of Fe 2p3, and the peaks located at 706.3, 707.3, 708.2, and 709.3 eV are attributed to the high spin of Fe^{2+} [45]. The relative concentration of the Fe element was calculated and depicted in Tables S1–S4.

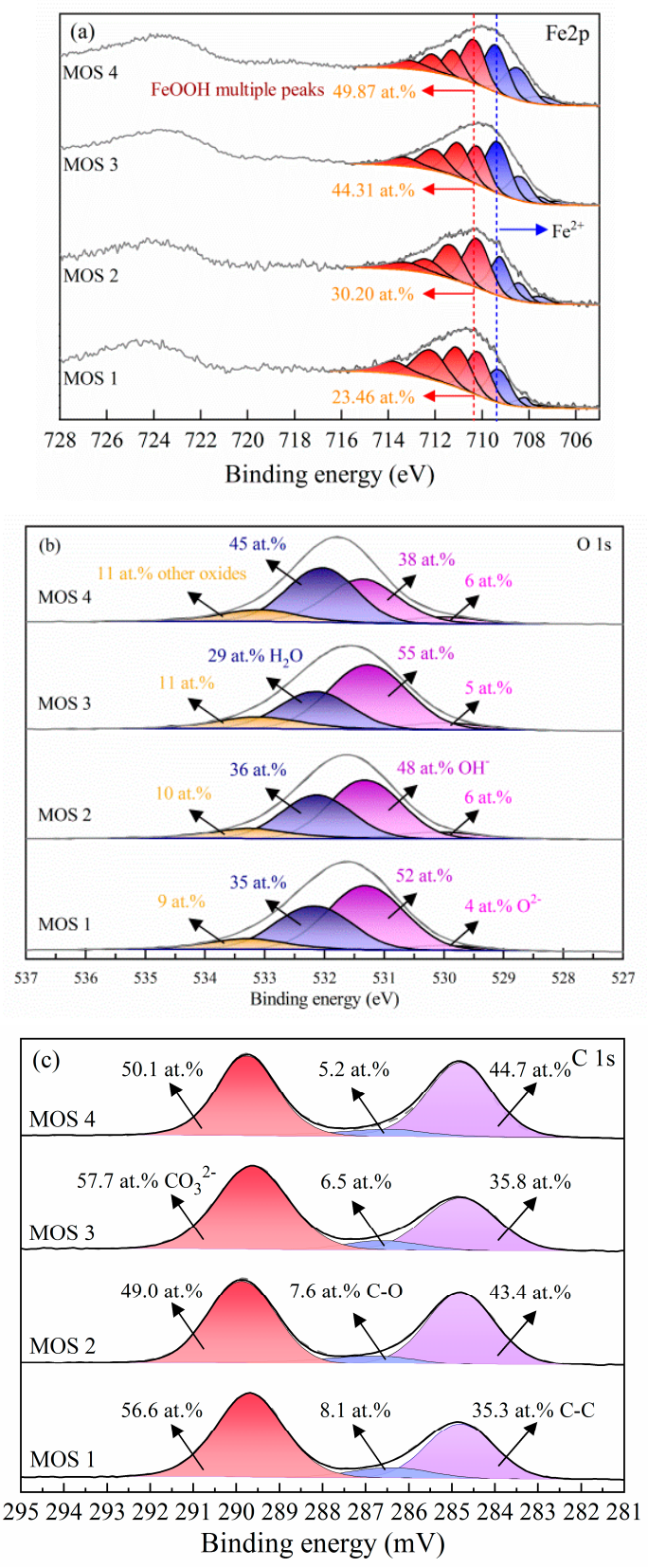

Figure 6. Fe 2p (**a**), O 1s (**b**), and C 1s (**c**) spectra recorded from the dolomite surface with 10^{-3} M Fe^{2+} without (MOS 1) and with 10^{-3} M SBX (MOS 2), and 10^{-2} M Fe^{2+} without (MOS 3) and with 10^{-3} M SBX (MOS 4) (pH = 8.5). RSF (Fe) = 14.353; RSF (O) = 2.881.

Approximately 23%–50% Fe^{2+} was observed on the modified mineral surface, which is believed to be because of the strong reducing potential of Fe^{2+} (Figure S11) [46,47]. It is well established that $[Fe(H_2O)_6]^{2+}$ (the first hydrolysate of Fe^{2+}) is stable under alkaline conditions and its continuous transformation to $Fe(OH)_2$ was a crucial source of Fe^{2+} [47]. The Eh-pH diagram (Figure S12) also indicated the existence of $Fe(OH)_2$. Further, the iron from the milling is also a favorable reductant that can prevent the oxidation of Fe^{2+} (inspired by the color of the flotation solution (Figure S13) [48], thus the considerable amount of Fe^{2+} absorbed on the dolomite surface [49].

Meanwhile, the binding energy at 710.4, 711.6, 712.8, and 713.8 eV fits well with the FeOOH structure, which confirmed that it shows strong adsorption with water molecules, and considerably weak interaction with xanthate (in other words, FeOOH cannot react with xanthate when water molecules exist), thus deteriorating the floatability [50]. As can be seen, the proportion of Fe^{2+} on the modified dolomite surface has nothing to do with the addition of SBX (considering the semi-quantitative capacity of XPS), but increases significantly with the initial Fe^{2+} concentration. This suggests that an obvious conversion between Fe^{2+} and Fe^{3+} by xanthate is not involved in this system.

O 1s spectra were also recorded to provide additional information on the Fe composition. As Figure 6b shows, O 1s peaks centered at 529.8, 531.3, 532.1, and 533.4 eV are recognized as O^{2-}, OH^-, adsorbed O (included H_2O molecules), and other oxides, respectively [51]. The quantitative concentration was presented in Tables S5–S8. Obviously, compared with O^{2-}, OH^- is the dominant formula of surface oxygen element. Considering the restrictions on the quantitative element concentration, the proportion of OH^- is reasonably consistent on the modified dolomite surface with or without treating with SBX. Interestingly, the OH^- distribution was similar to Fe species, which means that $Fe(OH)_2$ was a relative species (except FeOOH) on the modified dolomite surface.

Of course, the C 1s peaks were also recorded for identifying the Fe formula. As depicted in Figure 6c, selected peaks at 284.8, 286.5, and 289.8 eV are recognized as C-C, C-O, CO_3^{2-} species, respectively [52,53]. Considering the carbon contamination method in XPS measurements, C-C, and C-O species are attributed to the adventitious carbon. Meanwhile, the considerable amount of species at 289.8 eV is due to the formation of metal carbonates [53,54]. Because of the weak interactions between dolomite and xanthate, $FeCO_3$ is proposed as the other main active site on the modified dolomite surface. The calculated Eh-pH diagram (Figure S12) also demonstrates that $FeCO_3$ is the main formula of Fe^{2+} in carbonate solutions over a fairly wide potential range. As a result, the $FeCO_3$ species is another major ingredient that may contribute to dolomite floatability.

Above all, the formation of $Fe(OH)_2$ and $FeCO_3$ rather than FeOOH (weakly interaction with xanthate) may contribute to the extra floatability of modified dolomite. To clarify the selective adsorption of xanthate between FeOOH, $Fe(OH)_2$ and $FeCO_3$ (due to the low potential created by adding Fe^{2+} (−450 mV vs. SHE), xanthate cannot be oxidized to dixanthogen (50 mV vs. SHE, Figure S14) in this flotation system, so we just consider the effect of xanthate), the electron distributions of iron in different coordination fields were calculated by DFT and depicted in Figure 7. The possible reactions between Fe atoms in different crystals and xanthate are also annotated.

Xanthate is not generally used for the flotation of metal hydroxide. However, Rao's results [55] show that metal oxides can be floated by the long carbon chain xanthate. This can be explained by Chen's coordination model of flotation [28], where only the π electron pairs of Fe 3d orbit can react with the unoccupied π orbitals of xanthate (weak π-backbonding). As noted, the formation of π-backbonding is a covalent interaction, which is stronger than the other bonding. Figure 7 presented the calculated d electron arrangement of Fe ions in $Fe(OH)_2$, $FeCO_3$, and FeOOH. The detailed calculation parameters are listed in Supporting Information. Due to high spin properties, Fe^{3+} (d^5) does not have π electrons pairs in its electronic configuration. Nevertheless, the $Fe(OH)_2$ and $FeCO_3$ calculation results show that Fe^{2+} (d^6) in $Fe(OH)_2$ and $FeCO_3$ have one pair of π electrons in their t_{2g} orbitals, which reveals the difference between Fe atoms in these crystals. In particular, the

xanthate electronic configuration shows that it has unoccupied π orbitals. Consequently, the π electrons pairs in $Fe(OH)_2$ and $FeCO_3$ provide the possibility to interact with xanthate molecules (with Fe^{2+} coordinating with xanthate to form the weak π-backbonding), thus resulting in extra dolomite floatability when the $Fe(OH)_2$ and $FeCO_3$ existed.

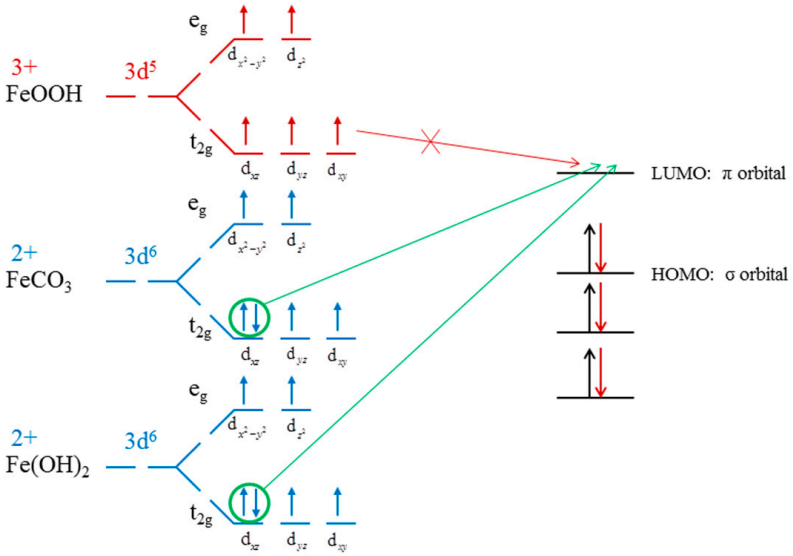

Figure 7. Coordination model of X^- [28], calculated ligand fields of Fe^{2+} in $Fe(OH)_2$ and $FeCO_3$, and Fe^{3+} in the ligand field of FeOOH [50].

For further verifying the prediction drawn by Chen's coordination model of flotation, DFT simulation calculations on the interactions between xanthate molecules and the $Fe(OH)_2/FeCO_3$ surface were conducted. The results are illustrated carefully as below (Figure 8):

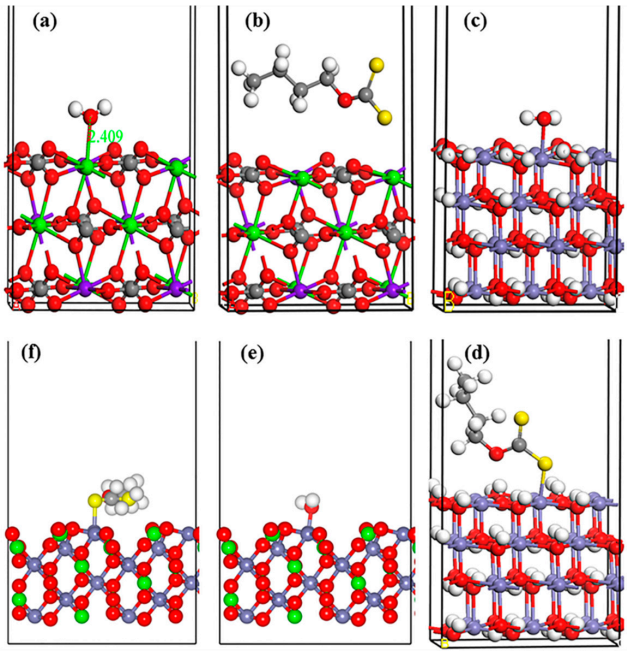

Figure 8. The most stable structures of water interact with the dolomite surface (**a**), xanthate reacts with the dolomite surface (**b**), water interacts with the $Fe(OH)_2$ surface (**c**), xanthate reacts with the $Fe(OH)_2$ surface (**d**), water interacts with the $FeCO_3$ surface (**e**), and xanthate reacts with the $FeCO_3$ surface (**f**). The O, C, H, Mg, Ca, and Fe atoms are represented as red, gray, white, purple, green, and lilac spheres, respectively.

3.5. Xanthate Molecule Adsorption on the Dolomite (101) Surface (DFT Simulation)

Considering the presented results, the absorbed $Fe(OH)_2$ and $FeCO_3$ may provide the opportunity for xanthate molecule adsorption, and improve its floatability. Thus, $Fe(OH)_2$ and $FeCO_3$ crystal and water molecules were employed to simulate xanthate molecular adsorption on a Fe^{2+}-absorbed dolomite surface [56]. The dolomite crystal consists of Ca^{2+} and Mg^{2+} layers sandwiched by CO_3^{2-} layers. We calculated the adsorption energies of small molecules on the (101) surface of $CaMg(CO_3)_2$ and $Fe(OH)_2$, and the (100) surface of $FeCO_3$, which are the primary cleavage surfaces [56–59]. The most stable crystal configuration is arranged in Figure 8. The interatomic distances are displayed in Table 1. In particular, due to the different mineral substrates, and different adsorbents on the same substrate, the interatomic distance cannot be regarded as the criterion (as adsorption energy) in determining the adsorption capacity.

Table 1. Adsorption energy and main interatomic distances (in Å) between adsorbates and slab surface (the lower of the adsorption energy values, the stronger of the adsorption capacity).

Surface + Adsorbate	Adsorption Energy (KJ/mol)	Ca-O (Å)	Mg-O (Å)	Fe-O (Å)	Fe-S (Å)
Dolomite Only	—	2.412	2.146	—	—
Dolomite + H_2O	−57.86	2.368	—	—	—
Dolomite+ Xanthate	0.35	—	—	—	—
$Fe(OH)_2$ + H_2O	−124.99	—	—	2.136	—
$Fe(OH)_2$ + Xanthate	−183.46	—	—	—	2.165
$FeCO_3$ +H_2O	−20.35	—	—	2.151	—
$FeCO_3$ +Xanthate	−113.38	—	—	—	2.529

Water molecule adsorption has been widely studied [55–57]. In this study, the H_2O can interact with the dolomite surface with −57.86 KJ/mol adsorption energy. Meanwhile, the Ca-O bond length is 2.368 Å (shorter than the Ca-O bond in dolomite). This means a strong interaction between H_2O and the dolomite surface occurs. Further, the dolomite surface shows higher affinity towards water molecules (−57.86 KJ/mol) than xanthate molecules (0.35 KJ/mol, the lower of the adsorption energy value, the stronger of the adsorption capacity), suggesting water molecules have a stronger interaction with the dolomite surface than xanthate molecules. However, astonishing results were presented when $Fe(OH)_2$ and $FeCO_3$ were introduced into this system. Figure 8c,d shows that $Fe(OH)_2$ surface displays a greater affinity towards xanthate (−183.46 KJ/mol) than H_2O (−124.99 KJ/mol), indicating the stronger adsorption of xanthate on the modified dolomite ($Fe(OH)_2$) surface. The same conclusion can be drawn in the $FeCO_3$-modified dolomite surface. Figure 8e,f depicts the selective adsorption of H_2O and xanthate on the $FeCO_3$ surface. The results revealed that the adsorption energy of xanthate (−113.38 KJ/mol) on the $FeCO_3$ surface is far below the H_2O adsorption energy (−20.35 KJ/mol), which shows the greater affinity of $FeCO_3$ towards xanthate than H_2O. The presented results verify the prediction made by Tof-SIMS and XPS analysis that $Fe(OH)_2$ and $FeCO_3$ can activate dolomite flotation due to the competitive adsorption of H_2O and xanthate between the dolomite, $Fe(OH)_2$ and $FeCO_3$ surfaces. This conclusion can be further confirmed by the partial density of state (PDOS) calculation.

The analysis of the PDOS results can provide a perspective of the interactions between molecules and crystals at the electronic level [56,60]. The DOS results of water and xanthate on $Fe(OH)_2$ and $FeCO_3$ crystal surfaces have been calculated (CASTEP module), and submitted in Figure 9. The Fermi energy (E_F = 0) had a value of 0 eV. As accepted, the density of state value at the Fermi level is a good indicator of the chemical reactivity. Significantly, the Fe 3d state in $Fe(OH)_2$ and $FeCO_3$ changed after interacting with H_2O and xanthate, indicating that the Fe atom is involved in the interactions between xanthate/water molecules and the $Fe(OH)_2$/$FeCO_3$ surface. Importantly, the Fe 3d state has the highest DOS value at the Fermi level (0 eV) when the Fe atoms interact with xanthate molecules,

demonstrating that the interaction of $Fe(OH)_2$ and $FeCO_3$ with the xanthate is stronger than that with H_2O. The PDOS results correspond well with the flotation tests, further validating the prediction by the coordination model of flotation, and provide favorable evidence for the activation mechanism of $Fe(OH)_2$ and $FeCO_3$ on dolomite flotation.

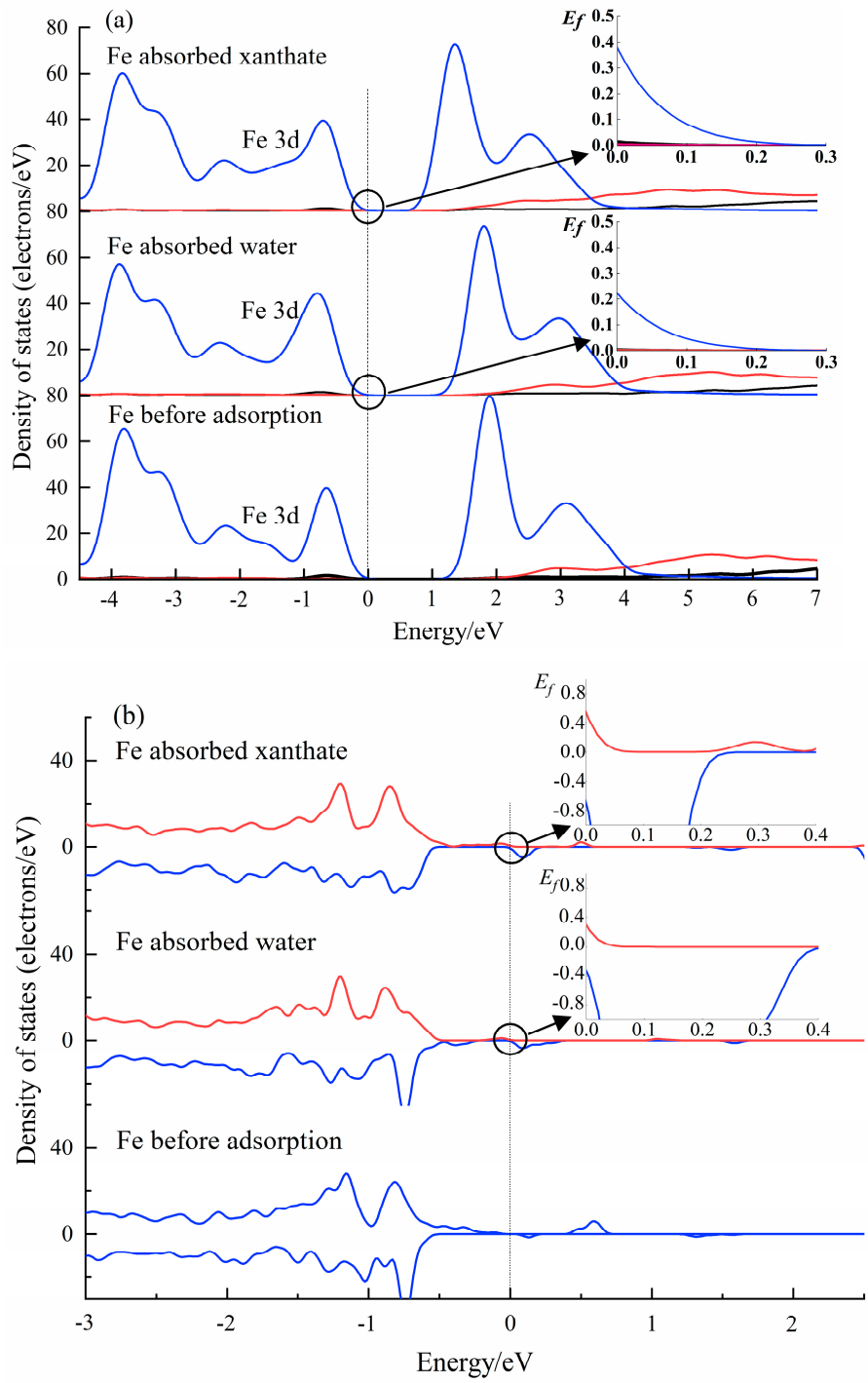

Figure 9. The calculated PDOS results of Fe 3d state in $Fe(OH)_2$ (**a**), and $FeCO_3$ (**b**) surface before and after the adsorption by adsorbents.

Figure 10 interprets the interactions of xanthate and air bubbles on the dolomite surface in the absence and presence of $Fe(OH)_2$ and $FeCO_3$. XPS analysis implied the formation of $Fe(OH)_2$, $FeCO_3$ and FeOOH after the addition of sufficient Fe^{2+}. The existence of $Fe(OH)_2$ is believed to be due to the strong reducing potential (Figures S11 and S12), and the iron

from the milling. According to the DFT simulation results and Chen's coordination model of flotation [28], the Fe^{2+} in $Fe(OH)_2$ and $FeCO_3$ crystals can interact more strongly with the S atoms in xanthate molecules than H_2O, and the absorbed xanthate molecules improve the hydrophobicity, thus increasing dolomite recovery.

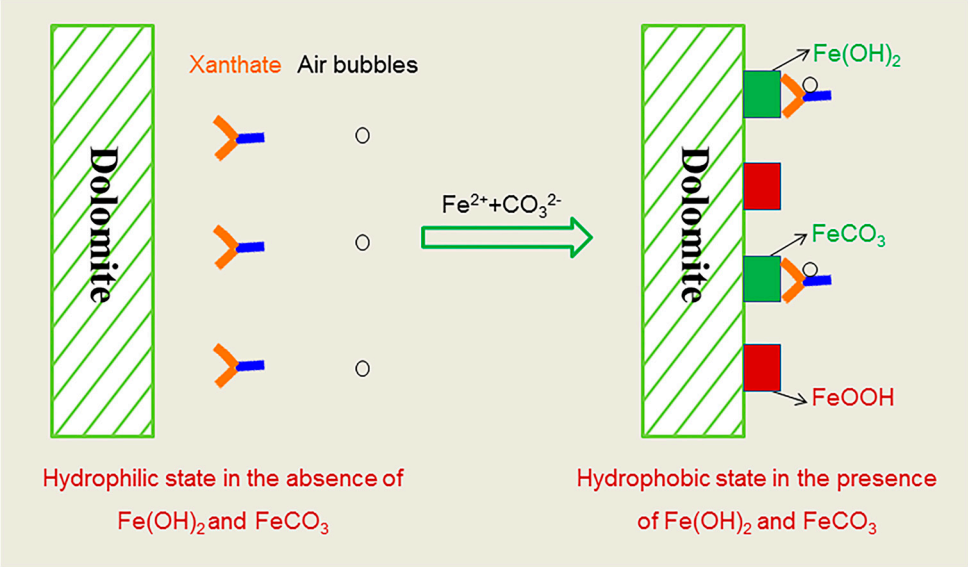

Figure 10. Schematic presentation of $Fe(OH)_2$ and $FeCO_3$ activated dolomite flotation.

4. Conclusions

The motivation of this investigation is the ambiguous knowledge on the high dolomite recovery in the flotation of Carlin-type gold deposits. Flotation tests suggested that Fe^{2+} rather than Fe^{3+} improved the floatability of dolomite, and dolomite recovery was reinforced with increasing the initial Fe^{2+} concentration. Both the contact angles and the thermodynamic results demonstrated that the effects of Fe^{2+} on the dolomite surface were much related to xanthate adsorption. Increasing Fe^{2+} concentration decreases the adsorption heat value, which indicates that Fe^{2+} promoted the adsorption of SBX on dolomite. Inspired by the Tof-SIMS and XPS data, the activated product on the modified dolomite surface are recognized as $Fe(OH)_2$ and $FeCO_3$. The coordination model of flotation showed that $Fe(OH)_2$ and $FeCO_3$ can interact with xanthate molecules (Fe^{2+} coordinates with S atoms in xanthate) with the formation of π-backbonding. DFT calculation indicated that $Fe(OH)_2$ displays a greater affinity towards xanthate (−183.46 KJ/mol) than H_2O (−124.99 KJ/mol) along with $FeCO_3$ (−113.38 KJ/mol adsorption energy with xanthate, and −20.35 KJ/mol adsorption energy with H_2O), absorbing xanthate molecules and improving dolomite hydrophobicity, resulting in extra dolomite floatability. The calculated PDOS results verify our conclusions at the electronic level. This study provides a comprehensive perspective for understanding and developing the poor selectivity between dolomite and pyrite in the flotation of Carlin-type gold deposits.

Supplementary Materials: The following supporting information can be downloaded at: https://www.mdpi.com/article/10.3390/min13020200/s1, Figure S1: GI-XRD patterns of dolomite (M 1: Dolomite, M 2: Ankerite); Figure S2. The size distribution of dolomite by laser particles analyzer (P90 = 60 μm); Figure S3. Effect of the SBX dosage on the modified dolomite recovery (pH = 8.5); Figure S4. Water recovery in dolomite flotation tests (pH = 8.5); Figure S5. Contact angles of dolomite in xanthate-containing solutions with different immersion; Figure S6. Zeta potential of dolomite under different reagent schemes ($c(Fe^{2+}) = 10^{-3}$ M, c(SBX) = 10^{-3} M); Figure S7. FTIR spectrum (400–3050cm^{-1}) of dolomite surface with different pretreatments (pH = 8.5, c(SBX) = 10^{-3} M); Figure S8. Accumulative normalized intensities of SBX adsorption on modified dolomite surface (pH = 8.5, c(SBX) = 10^{-3} M); Figure S9. Negative secondary (a), and Positive secondary ion (b, c) mass spectra collected from the purity dolomite (MS 1), dolomite treated with 10−3 M Fe^{2+} and SBX (MS 2),

dolomite treated with 3×10^{-3} M Fe^{2+} and SBX (MS 3), and dolomite treated with 10^{-2} M Fe^{2+} and SBX (MS 4) (pH = 8.5, c(SBX) = 10^{-3} M); Figure S10. Full range XPS spectra of dolomite treated with 0 M Fe^{2+} (a), 10^{-3} M Fe^{2+} (b), and 10^{-2} M Fe^{2+} (c) as the function of etching time (pH = 8.5, c(SBX) = 10^{-3} M SBX); Figure S11. The pulp potential of modified dolomite as the Fe^{2+} dosage (pH=8.5, c(SBX)=10^{-3} M); Figure S12. Eh-pH diagram of Fe-H_2O (a), and Fe-CO_3^{2-}-H_2O system at 25 °C (Fe as the main element, the activities of dissolved Fe are assumed to be 1 10^{-5} M); Figure S13. The picture of the dolomite pulp (pH = 8.5, c(Fe^{2+}) = 10^{-2} M, c(SBX) = 10^{-3} M); Figure S14. The calculated required potential for the xanthate oxidation under different concen-tration (pH = 8.5); Table S1. Fe fitting parameters of MOS 1 (Normalise Chi Sqr: 0.097718, Abbe Criteria: 0.4524); Table S2. Fe fitting parameters of MOS 2 (Normalise Chi Sqr: 0.073817, Abbe Criteria: 0.5516); Table S3. Fe fitting parameters of MOS 3 (Normalise Chi Sqr: 0.13833, Abbe Criteria: 0.7367); Table S4. Fe fitting parameters of MOS 4 (Normalise Chi Sqr: 0.098671, Abbe Criteria: 0.4037); Table S5. O and C fitting parameters of MOS 1 (Normalise Chi Sqr: 0.38167, Abbe Criteria: 0.53); Table S6. O and C fitting parameters of MOS 2 (Normalise Chi Sqr: 0.36445, Abbe Criteria: 0.7361); Table S7. O and C fitting parameters of MOS 3 (Normalise Chi Sqr: 0.24233, Abbe Criteria: 0.2225); Table S8. O and C fitting parameters of MOS 4 (Normalise Chi Sqr: 0.36997, Abbe Criteria: 0.5004) [61].

Author Contributions: H.Z.: conceptualization, methodology, software, and writing—original draft. X.N.: visualization, investigation, and editing. B.D.: supervision, validation, and editing. X.J.: data curation and supervision. R.R.: funding acquisition, supervision, and investigation. All authors have read and agreed to the published version of the manuscript.

Funding: This research was funded by Innovation Academy for Green Manufacture, Chinese Academy of Sciences.

Data Availability Statement: No availability statement.

Acknowledgments: The kind help of Chaoying Wang and Shifeng Tian, from Jingwei Hengrun Technology Co., LTD, Chongqing University and www.shiyanjia.com, respectively, is gratefully acknowledged in the way of English improvement, nanoscale etching and density function theory simulation.

Conflicts of Interest: No conflict of interest exists in the submission of this manuscript, and this manuscript is approved by all authors for publication.

References

1. Hassas, B.; Kappes, R.; Miller, J. Fundamental Surface Chemistry Aspects of Auriferous Pyrite Flotation with Carbon Dioxide and Nitrogen. Ph.D Thesis, The University of Utah, Salt Lake City, UT, USA, 2018.
2. Luo, X.; Yin, W.; Ma, Y.; Sun, C.; Yao, J. New Flotation Technology Research on Carbonate-containing Hematite. *Adv. Mater. Res.* **2012**, *454*, 210–215. [CrossRef]
3. Simmons, G.; Gathje, J. Method for processing gold-bearing sulfide ores involving preparation of a sulfide concentrate. *Miner. Eng.* **1998**, *11*, 307. [CrossRef]
4. Berninger, U.N.; Saldi, G.D.; Jordan, G.; Schott, J.; Oelkers, E.H. Assessing Dolomite Surface Reactivity at TemperatuRes. from 40 to 120 °C by Hydrothermal Atomic Force Microscopy. *Geochim. Cosmochim. Acta* **2016**, *199*, 130–142. [CrossRef]
5. Pokrovsky, O.S.; Golubev, S.V.; Schott, J. Dissolution kinetics of calcite, dolomite and magnesite at 25 °C and 0 to 50 atm pCO_2. *Chem. Geol.* **2005**, *217*, 3. [CrossRef]
6. Schott, J.; Pokrovsky, O.; Oelkers, E. The Link Between Mineral Dissolution/Precipitation Kinetics and Solution Chemistry. *Rev. Miner. Geochem.* **2009**, *70*, 1. [CrossRef]
7. Nunes, A.; Peres, A.; De Araujo, A.; Valadao, G. Electrokinetic properties of wavellite and its floatability with cationic and anionic collectors. *J. Colloid Interface Sci.* **2011**, *361*, 632–638. [CrossRef] [PubMed]
8. Chen, Y.; Zhang, G.; Shi, Q.; Yang, S.; Wang, M. Utilization of trisodium phosphate to eliminate the adverse effect of Mg^{2+} on the flotation of pyrite. *Miner. Eng.* **2020**, *150*, 106281. [CrossRef]
9. Mu, Y.; Peng, Y.; Lauten, R. The depression of pyrite in selective flotation by different reagent systems—A review. *Miner. Eng.* **2016**, *96–97*, 143–156. [CrossRef]
10. Li, R.; Li, Q.; Sun, X.; Li, J.; Wang, L. Removal of lead complexes by ferrous phosphate and iron phosphate: Unexpected favorable role of ferrous ions. *J. Hazard Mater.* **2020**, *392*, 122509. [CrossRef] [PubMed]
11. Azizi, D.; Larachi, F. Surface interactions and flotation behavior of calcite, dolomite and ankerite with alkyl hydroxamic acid bearing collector and sodium silicate. *Colloid Surf. A* **2017**, *537*, 126–138. [CrossRef]
12. Niu, X.; Ruan, R.; Xia, L.; Li, L.; Sun, H.; Jia, Y.; Tan, Q. Correlation of Surface Adsorption and Oxidation with a Floatability Difference of Galena and Pyrite in High-Alkaline Lime Systems. *Langmuir* **2018**, *34*, 2716–2724. [CrossRef]

13. Zeng, M.; Yang, B.; Guan, Z.; Zeng, L.; Luo, H.; Deng, B. The selective adsorption of xanthan gum on dolomite and its implication in the flotation separation of dolomite from apatite. *Appl. Surf. Sci.* **2021**, *551*, 149301. [CrossRef]
14. Yin, W.; Sun, H.; Hong, J.; Cao, S.; Yang, B.; Won, C.; Song, M. Effect of Ca selective chelator BAPTA as depressant on flotation separation of magnesite from dolomite. *Miner. Eng.* **2019**, *144*, 106050. [CrossRef]
15. Yu, J.; Ge, Y.; Guo, X.; Guo, W. The depression effect and mechanism of NSFC on dolomite in the flotation of phosphate ore. *Sep. Purif. Technol.* **2016**, *161*, 88–95. [CrossRef]
16. Jin, Y.; By, A.; Kc, A.; Hs, A.; Zz, A.; Wya, C.; Ns, A.; Qs, A. Sodium tripolyphosphate as a selective depressant for separating magnesite from dolomite and its depression mechanism. *Powder Technol.* **2021**, *382*, 244–253. [CrossRef]
17. Sun, H.; Yang, B.; Zhu, Z.; Yin, W.; Sheng, Q.; Hou, Y.; Yao, J. New insights into selective-depression mechanism of novel depressant EDTMPS on magnesite and quartz surfaces: Adsorption mechanism, DFT calculations, and adsorption model. *Miner. Eng.* **2020**, *160*, 106660. [CrossRef]
18. Yaoyang, R.; Zhang, Z.; Luo, H.; Xiao, C.; Zhou, F.; Chi, R. Effects of Metal Ions on the Flotation of Apatite, Dolomite and Quartz. *Minerals* **2018**, *8*, 141. [CrossRef]
19. Guo, J.; Zhou, Y. Transformation of heavy metals and dewaterability of waste activated sludge during the conditioning by Fe^{2+}-activated peroxymonosulfate oxidation combined with rice straw biochar as skeleton builder. *Chemosphere* **2020**, *238*, 124628. [CrossRef]
20. Yuan, L.; Shen, J.; Yan, P.; Zhang, J.; Wang, Z.; Zhao, S.; Chen, Z. Catalytic ozonation of 4-chloronitrobenzene by goethite and Fe^{2+}-modified goethite with low defects: A comparative study. *J. Hazard Mater.* **2019**, *365*, 744–750. [CrossRef]
21. Breitner, D.; Osán, J.; Fábián, M.; Zagyvai, P.; Szabó, C.; Dähn, R.; Marques Fernandes, M.; Sajó, I.E.; Máthé, Z.; Török, S. Characteristics of uranium uptake of Boda Claystone Formation as the candidate host rock of high level radioactive waste repository in Hungary. *Environ. Earth Sci.* **2015**, *73*, 1. [CrossRef]
22. Doi, A.; Ejtemaei, M.; Nguyen, A.V. Effects of ion specificity on the surface electrical properties of kaolinite and montmorillonite. *Miner. Eng.* **2019**, *143*, 105929. [CrossRef]
23. Tournassat, C.; Vinsot, A.; Gaucher, E.C.; Altmann, S. Chemical Conditions in Clay-Rocks. In *Developments in Clay Science*; Elsevier: Amsterdam, The Netherlands, 2015; Volume 6. [CrossRef]
24. Herman, J.S.; White, W.B. Dissolution kinetics of dolomite: Effects of lithology and fluid flow velocity. *Geochim. Cosmochim. Acta* **1985**, *49*, 10. [CrossRef]
25. Feng, Q.M.; Liu, G.S.; Zheng-Jun, Y.U.; Yi-Ping, L.U.; Le-Ming, O.U.; Zhang, G.F. Influence and mechanism of ferric and ferrous ions on flotation of talc. *J. Cent. South Univ.* **2006**, *37*, 3. [CrossRef]
26. Cao, Y.; Xie, X.; Tong, X.; Feng, D.; Song, Q. The activation mechanism of Fe(II) ion-modified cassiterite surface to promote salicylhydroxamic acid adsorption. *Miner. Eng.* **2021**, *160*, 106707. [CrossRef]
27. Chandra, A.P.; Gerson, A.R. A review of the fundamental studies of the copper activation mechanisms for selective flotation of the sulfide minerals, sphalerite and pyrite. *Adv. Colloid Interface Sci.* **2009**, *145*, 97–110. [CrossRef]
28. Chen, J. The interaction of flotation reagents with metal ions in mineral surfaces: A perspective from coordination chemistry. *Miner. Eng.* **2021**, *171*, 107067. [CrossRef]
29. Perdew, J.P.; Burke, K.; Ernzerhof, M. Erratum. Generalized Gradient Approximation Made Simple. *Phys. Rev. Lett.* **1996**, *77*, 3865. [CrossRef] [PubMed]
30. Perdew, P.J.; Chevary, A.J.; Vosko, H.S.; Jackson, A.K.; Pederson, R.M.; Singh, J.D.; Fiolhais, C. Erratum: Atoms, molecules, solids, and surfaces: Applications of the generalized gradient approximation for exchange and correlation. *Phys. Rev. B* **1993**, *48*, 7. [CrossRef] [PubMed]
31. Perdew, J.P.; Wang, Y. Accurate and simple analytic representation of the electron-gas correlation energy. *Phys. Rev. B* **1992**, *45*, 13244, Erratum in *Phys. Rev. B* **2018**, *98*, 079904. [CrossRef] [PubMed]
32. Luo, X.M.; Yin, W.Z.; Wang, Y.F.; Sun, C.Y.; Ma, Y.Q.; Liu, J. Effect and mechanism of dolomite with different size fractions on hematite flotation using sodium oleate as collector. *J. Cent. South Univ.* **2016**, *23*, 3. [CrossRef]
33. Jiang, L.C.; Wang, H.X.; Parekh, K.B.; Leonard, J.W. The surface and solution chemistry of pyrite flotation with xanthate in the presence of iron ions. *Colloid Surf. A* **1998**, *136*, 51–62. [CrossRef]
34. Sun, W.; Sun, C.; Liu, Q.R.; Cao, F.X.; Tao, H.B. Electrochemical behavior of galena and jamesonite flotation in high alkaline pulp. *Trans. Nonferr. Met. Soc.* **2016**, *26*, 2. [CrossRef]
35. Zhong, W.; Yin, W.; Wang, Y.; Yao, J. Selective flotation of magnesite from dolomite using α-chloro-oleate acid as collector. *Powder Technol.* **2020**, *373*, 147–151. [CrossRef]
36. Sun, Y.Q.; Yin, Z.W.; Cao, H.S.; Yang, B.; Sun, R.H.; Tang, Y.; Wang, H.D.; Yao, J. Adsorption kinetics and thermodynamics of sodium butyl xanthate onto bornite in flotation. *J. Cent. South Univ.* **2019**, *26*, 11. [CrossRef]
37. Yuasa, K.; Kumasaki, M.; Mizutani, T.; Arai, M. Thermal hazard evaluation procedure for detoxifying system of hazardous gases by using of reaction calorimeter. *J. Therm. Anal. Calorim.* **2008**, *93*, 41–45. [CrossRef]
38. Zhang, X.; Han, Y.; Gao, P.; Gu, X.; Li, Y. An Investigation into the Effects of Grinding Media on Grinding Products Characteristics and Flotation Performance of Pyrite. *Miner. Process. Extr. Metall. Rev.* **2020**, *42*, 367–373. [CrossRef]
39. Carbone, M.; Castle, E.J.; Ciriello, R.; Salvi, M.A.; Treacy, J.; Zhdan, P. In Situ Electrochemical–AFM and Cluster-Ion-Profiled XPS Characterization of an Insulating Polymeric Membrane as a Substrate for Immobilizing Biomolecules. *Langmuir* **2017**, *33*, 10. [CrossRef]

40. Gao, Z.; Zhang, J.; Zhang, S.; Wang, J.; Song, Y. Cationic etching of ZIF-67 derived $LaCoO_3/Co_3O_4$ as high-efficiency electromagnetic absorbents. *Chem. Eng. J.* **2020**, *421*, 127829. [CrossRef]
41. Bai, S.; Yu, P.; Li, C.; Wen, S.; Ding, Z. Depression of pyrite in a low-alkaline medium with added calcium hypochlorite: Experiment, visual MINTEQ models, XPS, and ToF–SIMS studies. *Miner. Eng.* **2019**, *141*, 105853. [CrossRef]
42. Lai, H.; Liu, Q.; Deng, J.; Wen, S.; Liu, Z. Surface chemistry study of Cu-Pb sulfide ore using ToF-SIMS and multivariate analysis—ScienceDirect. *Appl. Surf. Sci.* **2020**, *518*, 146270. [CrossRef]
43. An, B.A.; Deland, E.; Sobol, O.; Yao, J.; Skovhus, T.L.; Koerdt, A. The differences in the corrosion product compositions of Methanogen-induced microbiologically influenced corrosion (Mi-MIC) between static and dynamic growth conditions. *Corros. Sci.* **2021**, *180*, 109179. [CrossRef]
44. Yamashita, T.; Hayes, P. Analysis of XPS spectra of Fe^{2+} and Fe^{3+} ions in oxide materials. *Appl. Surf. Sci.* **2008**, *254*, 8. [CrossRef]
45. Biesinger, M.C.; Lau, L.W.; Gerson, A.R.; Smart, R.S.C. Resolving surface chemical states in XPS analysis of first row transition metals, oxides and hydroxides: Sc, Ti, V, Cu and Zn. *Appl. Surf. Sci.* **2010**, *257*, 887–898. [CrossRef]
46. Ojumu, T.V.; Petersen, J.; Hansford, G.S. The effect of dissolved cations on microbial ferrous-iron oxidation by Leptospirillum ferriphilum in continuous culture. *Hydrometallurgy* **2008**, *94*, 69–76. [CrossRef]
47. Wang, L.; Daub, K.; Qin, Z.; Wren, J. Effect of dissolved ferrous iron on oxide film formation on carbon steel. *Electrochim. Acta* **2012**, *76*, 208–217. [CrossRef]
48. Peng, Y.; Grano, S. Inferring the distribution of iron oxidation species on mineral surfaces during grinding of base metal sulphides. *Electrochim. Acta* **2010**, *55*, 19. [CrossRef]
49. Chen, J.; Yang, X.; Li, Y.; Liu, Y. Influences of electronic spin structures on the magnetic properties of Fe, Co and Ni ions and the adsorption of collectors. *Miner. Eng.* **2020**, *154*, 6. [CrossRef]
50. Niu, X.; Chen, J.; Li, Y.; Xia, L.; Li, L.; Sun, H.; Ruan, R. Correlation of surface oxidation with xanthate adsorption and pyrite flotation. *Appl. Surf. Sci.* **2019**, *495*, 143411. [CrossRef]
51. Nesbitt, H.W.; Muir, I.J. X-ray photoelectron spectroscopic study of a pristine pyrite surface reacted with water vapor and air. *Geochim. Cosmochim. Acta* **1994**, *58*, 21. [CrossRef]
52. Yang, J.; Liang, C. Investigation of changes in surface properties of bituminous coal during natural weathering processes by XPS and SEM. *Appl. Surf. Sci.* **2014**, *293*, 293–298. [CrossRef]
53. Heuer, J.K.; Stubbins, J.F. An XPS characterization of $FeCO_3$ films from CO_2 corrosion. *Corros. Sci.* **1999**, *41*, 7. [CrossRef]
54. Christie, A.B.; Sutherland, I.; Walls, J.M. An XPS study of ion-induced dissociation on metal carbonate surfaces. *Vacuum* **1981**, *31*, 513–517. [CrossRef]
55. Rao, S.R.; Finch, J.A. Base metal oxide flotation using long chain xanthates. *Int J. Miner. Process.* **2003**, *69*, 251–258. [CrossRef]
56. Escamilla-Roa, E.; Sainz-Díaz, C.I.; Huertas, F.J.; Hernandez-Laguna, A. Adsorption of molecules onto (1014) dolomite surface: An application of computational studies for microcalorimetry. *J. Phys. Chem. C* **2016**, *117*, 34. [CrossRef]
57. Liu, Y.; Chen, J.; Li, Y.; Zhang, J.; Kang, D. First-principles study on the adsorption structure of water molecules on a pyrite (100) surface. *Physicochem. Probl. Miner. Process.* **2021**, *57*, 121–130. [CrossRef]
58. Zhang, H.; Han, C.; Liu, W.; Hou, D.; Wei, D. The chain length and isomeric effects of monohydric alcohols on the flotation of magnesite and dolomite by sodium oleate. *J. Mol. Liq.* **2019**, *276*, 471–479. [CrossRef]
59. Li, L.; Zhang, C.; Yuan, Z.; Hao, H.; Zhao, C. Density Functional Theory and Atomic Force Microscopy Study of Oleate Functioned on Siderite Surface. *Minerals* **2018**, *8*, 33. [CrossRef]
60. Chen, J.H.; Lan, L.H.; Chen, Y. Computational simulation of adsorption and thermodynamic study of xanthate, dithiophosphate and dithiocarbamate on galena and pyrite surfaces. *Miner. Eng.* **2013**, *46*, 136–143. [CrossRef]
61. Frolova, L. Investigation of co-precipitation of Fe(II) and Ni(II) hydroxides. *Mater. Lett.* **2020**, *275*, 128065. [CrossRef]

Disclaimer/Publisher's Note: The statements, opinions and data contained in all publications are solely those of the individual author(s) and contributor(s) and not of MDPI and/or the editor(s). MDPI and/or the editor(s) disclaim responsibility for any injury to people or property resulting from any ideas, methods, instructions or products referred to in the content.